

Prepared for the Worst: A Learning-Based Adversarial Attack for Resilience Analysis of the ICP Algorithm

Ziyu Zhang¹, Johann Laconte¹, Daniil Lisus¹, and Timothy D. Barfoot¹

Abstract—This paper presents a novel method to assess the resilience of the Iterative Closest Point (ICP) algorithm via deep-learning-based attacks on lidar point clouds. For safety-critical applications such as autonomous navigation, ensuring the resilience of algorithms prior to deployments is of utmost importance. The ICP algorithm has become the standard for lidar-based localization. However, the pose estimate it produces can be greatly affected by corruption in the measurements. Corruption can arise from a variety of scenarios such as occlusions, adverse weather, or mechanical issues in the sensor. Unfortunately, the complex and iterative nature of ICP makes assessing its resilience to corruption challenging. While there have been efforts to create challenging datasets and develop simulations to evaluate the resilience of ICP empirically, our method focuses on finding the maximum possible ICP pose error using perturbation-based adversarial attacks. The proposed attack induces significant pose errors on ICP and outperforms baselines more than 88% of the time across a wide range of scenarios. As an example application, we demonstrate that our attack can be used to identify areas on a map where ICP is particularly vulnerable to corruption in the measurements.

I. INTRODUCTION

The Iterative Closest Point (ICP) algorithm has become a fundamental localization algorithm in mobile robotics [1] [2]. ICP computes a robot’s current pose by determining the transformation that optimally aligns the scan point cloud (robot’s current view) with a map point cloud. At the same time, lidar sensors have emerged as the predominant choice for robot localization and mapping [3]. However, despite its popularity, lidar-based ICP is prone to failures in challenging scenarios. Some scenarios, such as those with adverse weather conditions or significant occlusions, are challenging due to high levels of corruption in the lidar measurements. Corrupted measurements pose a significant safety threat, and they are the focus of this paper. Figure 1 illustrates how landmarks needed for localization can be occluded in typical autonomous driving conditions. With fewer landmarks to rely on, ICP can become more susceptible to other corruption in the measurements, leading to high estimate errors. Moreover, when an obstacle occludes landmarks in its proximity, ICP may wrongly identify it as part of the map. In such cases, ICP attempts to align the obstacle’s points in the scan to the map, leading to an error in the pose estimate. Similar errors can arise in adverse weather conditions. For instance, when the wind carries snow into the proximity of landmarks, it becomes difficult for ICP to distinguish and filter the snow from the landmarks.

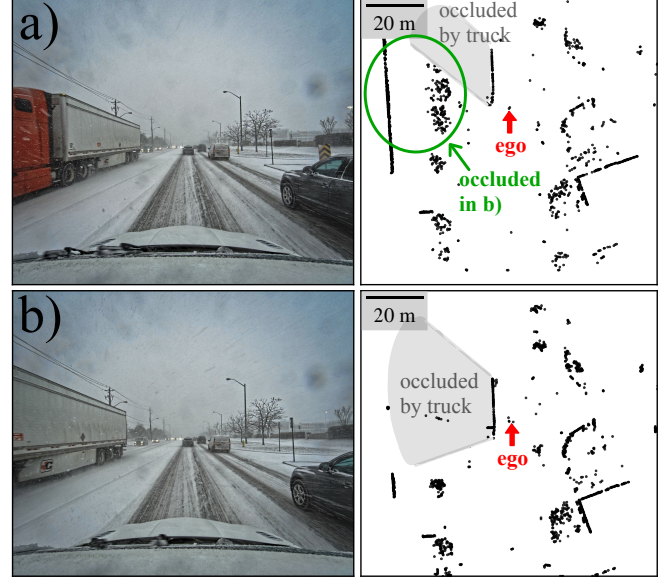


Fig. 1: Illustrative occlusion scenarios from the Boreas dataset [4] where the ego vehicle encounters occlusion caused by a truck. Camera images for two scenarios are shown on the left, with corresponding lidar scans captured at the same time on the right. Scenario a) precedes b) by 0.3 seconds. The ground planes in the lidar scans are removed for clarity. The pose of the ego vehicle and the region occluded by the truck are annotated with a red arrow and a gray sector, respectively. When the truck occludes the green-circled landmarks in b), the ICP algorithm may mistake the truck for the circled landmarks in its calculations, resulting in a significant error in the pose estimate.

To evaluate the resilience of ICP against corrupted measurements, adverse weather datasets such as Boreas [4] and CADC [5] have been collected. Prior works [6] [7] have evaluated ICP on these datasets. Additionally, Endo *et al.* [8] simulated occlusion cases in cities and used them to evaluate the performance of lidar-based localization algorithms under occlusion. This paper presents a novel way to evaluate ICP’s resilience by estimating the maximum pose error that may result from corrupted measurements at a given location. Finding the maximum possible error allows us to set a safe lower bound on ICP’s resilience. Moreover, knowing the maximum possible error before deployment can help avoid high-error locations when deploying autonomous robots.

While Laconte *et al.* [9] previously presented an analytic approach to bridge this gap, we propose a learning-based approach with the advantage of requiring fewer assumptions and approximations. Following [9], we abstract the problem

¹ University of Toronto Institute for Aerospace Studies (UTIAS), 4925 Dufferin St, Ontario, Canada. {char.zhang, johann.laconte, daniil.lisus}@robotics.utias.utoronto.ca, tim.barfoot@utoronto.ca

by modeling corruption as measurement perturbations. Specifically, we train a generative network to perturb lidar points to maximize the ICP pose error. This network can then be used to estimate the highest possible pose error at a location subject to a certain extent of measurement perturbations. We evaluate our approach by attacking point-to-plane ICP on the ShapeNetCore [10] and Boreas [4] datasets. Our approach consistently outperforms heuristic baselines and detects dangerous locations the current analytical state-of-the-art method misses. Our contributions are:

- To the best of our knowledge, we propose the first learning-based adversarial attack on lidar-based ICP. Our approach can generate adversarial point clouds in one forward pass and demonstrates strong attack performance.
- We present a novel way to estimate the worst ICP pose error that can arise at a location subject to a given amount of perturbation in the measurements.
- As ICP’s resilience to corruptions is location-dependent, we demonstrate, through extensive experiments on the Boreas dataset [4], the feasibility of using our approach to identify, pre-deployment, dangerous locations to avoid.

II. RELATED WORK

A. Analysis on ICP in Challenging Environments

When robots are deployed in the real world, they must operate robustly in challenging situations. Environments particularly challenging to ICP include those with geometric degeneracy, occlusions, and adverse weather conditions.

Geometrically under-constrained environments refer to environments with very limited or degenerate geometric constraints for registration such as tunnels and narrow corridors. Under-constrained environments have long been established as a major source of ICP error [11]. Numerous degeneracy detection techniques and degeneracy-aware localization methods have been proposed [12]. Scenarios such as occlusions and adverse weather, on the other hand, are challenging due to high levels of corruption in the lidar measurements. Corrupted measurements pose a significant safety threat, and they are the focus of this paper.

To make registration algorithms including ICP robust to noisy measurements, numerous outlier filters have been proposed. Babin *et al.* [13] give a comprehensive analysis of the popular outlier filters. Although outlier filters can mitigate the influence of outliers, their negative effects can persist in the worst cases [6]. Another line of research suggests to address this problem via de-noising the measurements. For instance, Charron *et al.* [14] presented a method to remove the noise in 3D lidar point clouds caused by snow. Our work aims to quantify and understand the impact of corrupted measurements on ICP. Putting lidar-based localization to the test, Burnett *et al.* [7] conducted an extensive evaluation of a lidar-based localization system on the all-weather Boreas dataset [4]. They found that lidar-based localization is surprisingly robust to moderate precipitation. Later, Courcelle *et al.* [6] evaluated lidar-based ICP over the Canadian Adverse Driving Conditions (CADC) dataset [5] and also discovered that lidar-based ICP is robust to a high level of precipitation. However, they observed

that extreme, abrupt cases such as snow gusts led to significant ICP localization errors. Due to an insufficient amount of data on these extreme cases, they could not quantitatively evaluate the impact of these extreme events on ICP.

Courcelle *et al.* [6] identified view obstruction (occlusion) as another event that led to large pose errors. Endo *et al.* [8] presented a comprehensive evaluation of lidar-based localization under occlusions through simulation. Unsurprisingly, they found that, on average, localization error increases with the percentage of the scene being occluded and significant localization errors can arise when half or more of the scene is occluded.

Most similar to our work, Laconte *et al.* [9] proposed a closed-form method for estimating the maximum expected ICP error from a sector of corrupted measurements. Laconte *et al.* [9] then assess ICP’s resilience by finding the smallest sector of corruption that can cause significant errors. This paper proposes an alternative solution that removes three key assumptions of [9]: 1) single-iteration ICP, 2) known data associations, and 3) robust filters are not used. A more detailed analysis and empirical comparison can be found in Section IV-D.4. Similar to [9], our approach can pinpoint dangerous locations where significant localization errors can occur if lidar measurements are corrupted. Unlike degeneracy detection methods [15], which predict the localizability of a location under normal conditions, we account for the possibility of measurement corruptions. A location can have enough geometric constraints yet still experience significant pose errors when the measurements are corrupted.

B. Adversarial Attacks Against Autonomous Driving Systems

Adversarial attacks that deliberately craft examples to undermine the target algorithm’s performance are very suitable for our purpose of worst-case analysis. Many point cloud adversarial attacks have been proposed against different components of the autonomy stack. Yang *et al.* [16] introduced novel frameworks for attacking algorithms processing 3D point clouds. These attacks work via point addition, point removal, and gradient-based point perturbation. Zhou *et al.* [17] proposed the first generative attack against point cloud classification algorithms via point perturbation. They showed that generative approaches are much faster than gradient-based approaches while upholding good attack performance. For this reason, and the resemblance of our task to theirs, our architecture draws inspiration from theirs.

In the object detection domain, Sun *et al.* [18] discovered that detection models tend to ignore occlusion patterns in the point clouds and introduced a black-box attack exploiting this vulnerability. Zhang *et al.* [19] proposed an attack that perturbs vehicle trajectories to maximize the errors of trajectory prediction algorithms. They also leveraged the attack to assess how worst-case predictions would affect downstream tasks. They successfully increased the prediction errors by more than 150% and showed that worst-case predictions have critical safety concerns. Their work supports our proposal of using adversarial attacks for worst-case performance analysis. While we draw inspiration from these works, they are not

attacking localization algorithms. For attacks against localization algorithms, Wang *et al.* [20] presented how to use infrared light to mislead camera-based SLAM. On lidar-based SLAM specifically, Xu *et al.* [21] demonstrated the feasibility of introducing false loop-closure detection by increasing the similarity between two distinct locations using physical objects. Our work differs from these works in that we are not merely introducing errors in the target algorithm but rather maximizing its error. Moreover, their target algorithms and attack mechanisms significantly differ from ours.

Similar to our work, Yoshida *et al.* [22] proposed a method for misleading lidar-based ICP to a specific wrong pose via adversarial point perturbation. While both [22] and our work are adversarial attacks on ICP, the attack objectives differ. Yoshida *et al.* [22] aim to corrupt the scan to mislead ICP to output a given incorrect pose that the adversary desires. These incorrect poses are neither designed nor guaranteed to maximize ICP errors. Our attack, in contrast, learns to corrupt the scan to maximize ICP errors. Therefore, unlike [22], ours can estimate the maximum pose error that may result from a given extent of perturbations in the scan. Besides, their method is iterative and gradient-based, while ours is learning-based. As shown in [17], learning-based approaches are much faster. [22] is also limited to 2D lidar scans and tampers only with the distance, not the angle, of points. Our work operates on both 2D and 3D lidar scans and can perturb both the distance and the angle.

III. THEORY

This section details the attack target, model architecture, and loss functions used for training. Our attack pipeline, which is the same during training and testing, is visualized in Figure 2. We propose a generative network that learns how to perturb a point cloud to maximize the pose error of ICP while keeping the perturbations within a specified bound.

A. Attack Target: ICP

Our model can attack any lidar-based ICP algorithm. However, we need differentiable versions of ICP to train. We train using dICP [23], which supports differentiable ICP and the use of outlier filters. Note that we attack the single-frame ICP algorithm on its own, rather than a full localization pipeline (e.g., with odometry), which we leave for future work.

Given a reference point cloud (also known as the map) $Q \in \mathbb{R}^{M \times 3}$ and a measured point cloud (also known as the scan) $P \in \mathbb{R}^{N \times 3}$, ICP estimates a transform from the scan to the map $\hat{T}_{QP} \in SE(3)$. $M, N \in \mathbb{N}$ denote the number of points in the map and scan, respectively. The ICP pose error vector $\xi \in \mathbb{R}^6$ can be calculated using the ground truth transform $T_{QP} \in SE(3)$ via

$$\xi = \begin{bmatrix} \rho \\ \phi \end{bmatrix} = \log \left(\hat{T}_{QP} T_{QP}^{-1} \right)^\vee, \quad (1)$$

where $\rho \in \mathbb{R}^3$ is the translation component of the error and $\phi \in \mathbb{R}^3$ is the rotation component of the error. Here, $\log(\cdot)$ maps an $SE(3)$ element to its lie algebra $\mathfrak{se}(3)$ and $(\cdot)^\vee$ maps an $\mathfrak{se}(3)$ element to \mathbb{R}^6 [24].

B. Attack model

Our model is a generator G consisting of an encoder and a decoder. The encoder is based on PointNet++ [25] [26] and learns to extract hierarchical features from an input point cloud $X \in \mathbb{R}^{N \times 3}$. Using the extracted features, the decoder learns how to perturb X to get $X_{\text{adv}} \in \mathbb{R}^{N \times 3}$. This architecture is inspired by LG-GAN [17], which successfully attacked 3D point cloud classification algorithms via perturbation.

1) *Encoder*: Hierarchical features provide rich representations of the point cloud, encompassing global and local aspects. To extract hierarchical features, we design the encoder with four cascaded PointNet++ [25] set-abstraction modules, as shown in Figure 2. A set-abstraction module takes a set of points and samples a smaller set using farthest-point sampling. Every sampled point embeds local patterns around it by learning to effectively aggregate features of its neighboring points in the original set. Subsequently, this subset of points along with newly learned features are fed into the next set-abstraction module. By stacking set-abstraction modules one on top of another, a hierarchy of features of various scales can be extracted. Precisely, the encoder extracts features of four scales: $F_1 \in \mathbb{R}^{N \times 64}$, $F_2 \in \mathbb{R}^{\frac{N}{a} \times 128}$, $F_3 \in \mathbb{R}^{\frac{N}{b} \times 256}$, and $F_4 \in \mathbb{R}^{\frac{N}{c} \times 512}$ where $a, b, c \in \mathbb{R}$ are manually selected hyperparameters.

2) *Decoder*: When decoding, we want to leverage information at all scales. However, higher-level features are sparser and not available for every point in the original point cloud X . Therefore, F_2 , F_3 , and F_4 are interpolated. The procedure for interpolation is as follows. For every point in X , higher-level features of k -nearest neighbors are weighted inversely-proportionally to their distances and summed. These weighted sums are passed through neural network layers, which turn the features into more compact sizes of $N \times 64$. Finally, interpolated $F'_2, F'_3, F'_4 \in \mathbb{R}^{N \times 64}$ are concatenated with F_1 and X , and the result is passed through four 1D convolution layers to generate the adversarial point cloud X_{adv} .

C. Loss function

The loss function is a weighted sum of two component losses: adversarial loss \mathcal{L}_{adv} and reconstruction loss \mathcal{L}_{rec} . That is

$$\mathcal{L} = \alpha \mathcal{L}_{\text{adv}} + \beta \mathcal{L}_{\text{rec}}, \quad (2)$$

where $\alpha, \beta \in \mathbb{R}$ are manually selected hyperparameters. The adversarial loss guides the generator G to generate the adversarial point cloud X_{adv} that is optimized to maximize the ICP pose error. Therefore, \mathcal{L}_{adv} is defined as

$$\mathcal{L}_{\text{adv}} = - \left\| \begin{bmatrix} w_1 \\ w_2 \\ w_3 \end{bmatrix} \odot \rho \right\|_2 - \left\| \begin{bmatrix} w_4 \\ w_5 \\ w_6 \end{bmatrix} \odot \phi \right\|_2 \quad (3)$$

where \odot is the element-wise multiplication operator. Manually selected hyperparameters $w_i \in \mathbb{R}$ for $i = 1, \dots, 6$ specify the weights of the pose error elements. The ICP error is split into the translation component $\rho \in \mathbb{R}^3$ and the rotation component $\phi \in \mathbb{R}^3$ due to differences in scale and physical representation.

To better assess the real-world ICP deployment risks, we introduce a loss \mathcal{L}_{rec} that binds the perturbations G can

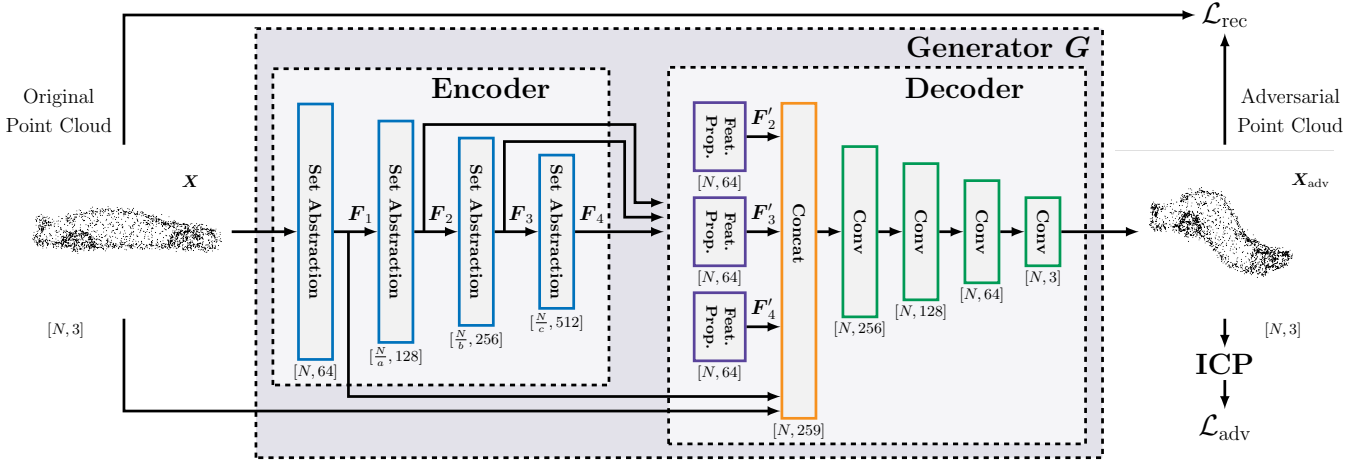


Fig. 2: Overview of the proposed attack pipeline. Given an input point cloud \mathbf{X} , the encoder extracts hierarchical features from it using set-abstraction modules from the PointNet++ [25] architecture. The decoder interpolates the extracted features and uses them along with the original point cloud to produce an adversarial point cloud \mathbf{X}_{adv} to attack ICP. The encoder and decoder together form the generator \mathbf{G} , which is trained using reconstruction loss and adversarial loss.

introduce. The ICP algorithms are often equipped with outlier filters, rendering extreme perturbations ineffectual in maximizing pose errors. However, there remain other reasons to constrain the perturbations further. Certain real-world events may only cause perturbations up to a realistic threshold. Moreover, there may be downstream ICP failure detectors that would disregard ICP’s outputs, if the perturbations exceed a certain magnitude. In this case, one can constrain the perturbations, using \mathcal{L}_{rec} , to find the maximum ICP error that can escape detection. For these reasons, a loss \mathcal{L}_{rec} is introduced to constrain the perturbations as needed.

$$\mathcal{L}_{\text{rec}} = \frac{1}{N} \sum_{i=1}^N S(\|\mathbf{x}_i - (\mathbf{x}_{\text{adv}})_i\|_2)^2, \quad (4)$$

where \mathbf{x}_i is a point in the scan \mathbf{X} and $(\mathbf{x}_{\text{adv}})_i$ is the corresponding point in \mathbf{X}_{adv} . $S(\cdot)$ is the SoftShrinkage function defined as

$$S(z) = \begin{cases} z - \lambda, & \text{if } z > \lambda \\ z + \lambda, & \text{if } z < -\lambda \\ 0, & \text{otherwise.} \end{cases} \quad (5)$$

The customizable parameter $\lambda \geq 0$ represents the perturbation bound.

Once trained, \mathbf{G} can estimate the maximum pose error that can arise at a location with up to λ units (usually meters) of perturbation in the measurements.

IV. EXPERIMENTS

This section presents qualitative and quantitative results on the ShapeNetCore [10] and Boreas [4] datasets. Implementation details for the two datasets differ and are documented separately. We compare our method with heuristic baselines to show that our model learns non-trivial perturbations and showcases strong attack performance. Then, we compare it with the state-of-the-art method to demonstrate the viability and benefits of using our approach to identify dangerous locations.

A. Datasets

We evaluate our attack on two datasets — ShapeNetCore [10] and Boreas [4]. The ShapeNetCore dataset is a subset of the ShapeNet dataset that contains 3D models of simple objects. We follow [27]’s procedures to sample points from the 3D models and generate normals. We use ShapeNetCore to understand visually the perturbations our model learns. Consequently, we cast the 3D ShapeNetCore point clouds to 2D. As ShapeNetCore objects vary significantly in size, we normalize the point clouds to fit within a unit circle centered at the origin for an easier parameter selection. We use the full point clouds as maps and randomly sample 2,048 points from the maps to create scans. We add normally distributed noise with a zero mean and a 0.025 standard deviation to the scans to avoid unrealistically perfect alignment. Finally, a small, random transformation is applied to each scan. The transformation consists of uniformly distributed translations from -0.08 to 0.08 (unitless due to normalization) along the x -axis and the y -axis as well as a uniformly distributed rotation from -10 to 10 degrees around the z -axis. This transformation serves as the ground truth pose. The transformations are kept small such that the ICP algorithm can use no motion for its initial guesses.

To assess our attack’s effectiveness for autonomous navigation applications, we further evaluate our attack on the Boreas dataset [4], an all-weather autonomous driving dataset collected by driving a repeated route over one year. The Boreas dataset is chosen for its abundant data with occlusions and adverse weather. We use the Teach and Repeat [28] framework to establish localization pairs on the Boreas dataset, following the procedure described in [7]. Teach and Repeat first conducts a teach pass along a route to construct a map, to which the subsequent repeat passes along the same route can be localized. The sequence of lidar point clouds gathered during the teach pass is processed into submaps. The sequences of lidar point clouds captured during the repeat passes, the “live scans”, are localized against the spatially closest submaps. Once localization pairs are generated, we

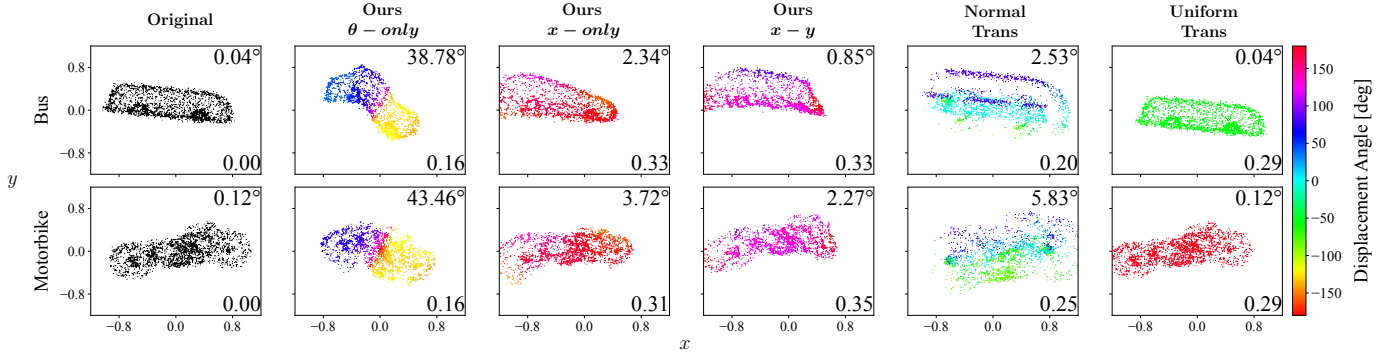


Fig. 3: A qualitative comparison between the original point clouds and the adversarial point clouds produced by our model and the baselines. Columns 2 through 6 showcase the adversarial point clouds resulting from applying our models and the baselines to the original point clouds in column 1. The adversarial point clouds are coloured according to the angle of the displacement vectors, $\mathbf{X}_{\text{adv}} - \mathbf{X}$. The heading pose error and the norm of the lateral and longitudinal pose errors of ICP induced by each point cloud are indicated at the upper and lower right corners, respectively. The lateral and longitudinal pose errors are unitless as the point clouds are normalized. Minor ICP pose errors are observed even when localizing the uncorrupted point clouds in column 1. This occurs because noise is added to the scans to prevent perfect alignment between the scans and the maps.

preprocess them to use for training our network. First, we align the live scans with the corresponding submaps using the ground truth poses. The ground truth poses are provided by the Global Navigation Satellite System. Then we apply a small, random transformation to each live scan to generate the final scan we task ICP to localize. The transformations involve random translations, uniformly distributed from -0.3 to 0.3 meters, along the x -axis, y -axis, and z -axis, as well as random rotations, uniformly distributed from -10 to 10 degrees, around the x -axis, y -axis, and z -axis.

B. Baselines

Given the absence of established baselines in both ICP worst-case analysis and adversarial attacks against ICP, we compare our approach with straightforward yet effective heuristic baselines.

1) *Uniform Translation Baseline*: The first baseline we adopt uniformly translates the entire scan by the maximum allowed perturbation, λ , at random angles in the $x-y$ plane. The perturbations are restricted to the $x-y$ plane because we focus on the lateral and longitudinal localization errors a model can induce. These errors are more significant than vertical pose errors in autonomous navigation applications.

2) *Normal Translation Baseline*: Another baseline we compare to moves points in the scan by λ in the direction of their normal vectors projected onto the $x-y$ plane. We hypothesize that this will be more effective than the uniform translation baseline in attacking point-to-plane ICP, which aims to minimize the normal distance from each point in the scan to the tangent plane of the corresponding point in the map. Moreover, [9] shows that shifting measured points along the normal vectors of their associated map points is an effective attack on point-to-plane ICP.

As the normal vectors are bidirectional, we need to unify their directions. When the x -component of the normal vector is zero, the vector is flipped such that its y -component is positive. When the x -component is non-zero, the vector is flipped such that its x -component is positive.

C. ShapeNetCore Results

1) *Implementation Details*: We train our models on approximately 8,900 ShapeNetCore samples using a batch size of 32. We determine empirically that the optimal values for hyperparameters a, b, c are 2, 4, 8, respectively, conditioned on the rest of our settings. For \mathcal{L}_{adv} , we set $\alpha = 1$ and $\beta = 10$. It takes 10 to 14 epochs (i.e., 2 to 2.5 hours on an NVIDIA Tesla V100 DGXS 32GB GPU) to converge. We use the AdamW [29] optimizer with a StepLR scheduler that reduces the initial learning rate of 10^{-4} by 30% every 7 epochs. Before training, we pretrain the generator for 50 epochs on the training dataset with $\alpha = 0$ and $\beta = 1$, essentially asking it to reconstruct the original scans. Without pretraining, the generator generates scans that are too different from the maps to extract meaningful gradients from ICP.

The ICP algorithm under attack is of type point-to-plane. We limit its maximum number of iterations to 25 to expedite training. For testing, we set the maximum number of iterations to 150, which we verify to be more than enough for ICP to converge with an error tolerance of 10^{-4} in most cases. Samples where ICP does not converge are dropped. The ICP algorithm is also equipped with a Cauchy robust filter with the Cauchy parameter set to 0.15 and a maximum distance filter [30] with $d_{\text{max}} = 0.3$. These parameters are chosen according to common practices.

2) *Case Study on Weights in the Adversarial Loss*: This section explores how weights in the adversarial loss (3) affect the kind of perturbations our model learns. We train our model on the ShapeNetCore dataset in three settings. In the θ -only setting, we set $w_6 = 1$ and all other weights $w_1 = w_2 = w_3 = w_4 = w_5 = 0$. The x -only setting uses only the x -axis translation error in \mathcal{L}_{adv} by setting $w_1 = 1$ and all other weights to 0. Finally, the $x-y$ setting uses both x -axis and y -axis translation errors in \mathcal{L}_{adv} (i.e., $w_1 = w_2 = 1$ and $w_3 = w_4 = w_5 = w_6 = 0$).

We then use models trained in these three settings to attack different types of objects. Examples of the resulting adversarial point clouds are shown in Figure 3 and Figure 6. Figure 3 and

Method	$\lambda = 1$ m		$\lambda = 2$ m		$\lambda = 3$ m		$\lambda = 4$ m		$\lambda = 5$ m	
	Trans Pose Error [m]	% Ours is Larger	Trans Pose Error [m]	% Ours is Larger	Trans Pose Error [m]	% Ours is Larger	Trans Pose Error [m]	% Ours is Larger	Trans Pose Error [m]	% Ours is Larger
Original	0.07 ± 0.21	99.72%	0.07 ± 0.21	99.85%	0.07 ± 0.21	99.91%	0.07 ± 0.21	99.94%	0.07 ± 0.21	99.96%
Uniform	1.16 ± 0.16	99.13%	2.17 ± 0.14	98.98%	3.14 ± 0.18	98.48%	4.12 ± 0.29	97.43%	5.07 ± 0.48	96.98%
Normal	1.31 ± 0.20	98.17%	2.50 ± 0.32	96.65%	3.57 ± 0.56	94.58%	4.49 ± 0.91	90.07%	5.21 ± 1.29	88.28%
Ours	1.86 ± 0.48	-	3.21 ± 0.63	-	4.47 ± 0.79	-	5.49 ± 0.89	-	6.48 ± 1.00	-

TABLE I: Translation pose errors (higher is better) induced by our method and baselines under different perturbation bounds. “Uniform” and “Normal” refer to the uniform and normal translation baselines, respectively. The “% Ours is Larger” column lists the percentage of time our model induces a larger translation pose error than the models in comparison. Translation pose errors are listed in mean \pm standard deviation. Only longitudinal and lateral pose errors are considered. The results are based on four Boreas repeat passes along the same route under varying weather conditions, including piled snow, snowing, and rain.

6 show that our model perturbs both the distance and the angle of points. In the motorbike example, our θ -only model moves the back wheel from the third quadrant to the second quadrant, changing the angle of these points. Our model trained under the θ -only setting introduces perturbations that can be largely characterized as rotations. Moreover, adversarial point clouds generated under this setting induce much higher rotational pose errors compared to other settings, which aligns with our expectations. When trained under the x -only setting, our model, instead of rotating, shifts the original point clouds to the left, inducing pose errors in the x direction. When we introduce y -axis pose errors into the adversarial loss in the $x-y$ setting, our model, in addition to shifting the original point clouds to the left, shifts the point clouds upward as well.

3) *Comparison with Baselines:* In this section, we compare the perturbations introduced by the baselines with those learned by our model in the $x-y$ setting. The baselines and our model in the $x-y$ setting are subject to the same λ to enable comparison. The normal translation baseline moves every point along its normal vector, which results in different geometric features being translated in different directions. The uniform translation baseline translates the entire point cloud at random angles. As indicated by the colour, our method does not translate all points in the same direction as the uniform translation baseline. In the bus example, ours warps the bus while translating the two ends of the bus to the left and shifting the center of the bus upward and leftward. These subtle differences set our model apart from simple heuristics and enable it to outperform them. Figure 3 and 6 indicate that our method induces higher pose errors than both baselines when allowed the same amount of perturbation.

D. Boreas Results

1) *Implementation Details:* We train our models using 20,000 samples drawn from two Boreas repeat sequences associated with the same teach sequence. We test on four Boreas repeat sequences, approximately 32km of driving data, associated with the same teach sequence. The training batch size is 6. The Boreas live scans are much denser than the ShapeNetCore point clouds. Input point clouds to G have sizes of $10,000 \times 3$. The point clouds are kept in 3D. For these denser point clouds, we find the optimal values of a, b, c change to 3, 12, 48, respectively. We again use $\alpha = 1$ and $\beta = 10$ where α and β represent the weights of the adversarial

and reconstruction losses, respectively, in the loss function. We find that using a small value for β significantly increases the magnitudes of the pose errors our model can induce. We train for 8 to 10 epochs (~ 34 hours) on an NVIDIA Tesla V100 GPU, with an AdamW optimizer. The learning rate is set to 10^{-4} initially and reduced by 30% every 5 epochs. Pretraining of G for 3 epochs is also done before the actual training. For experiments in Section IV-D on the Boreas dataset, all of our models are trained under the $x-y$ setting.

The ICP algorithm under attack is of type point-to-plane, with the maximum number of ICP iterations capped at 25 to expedite training. For testing, we set the maximum number of iterations to 100, which is sufficient for ICP to converge in the majority of cases with a tolerance of 10^{-4} . Test samples where ICP does not converge are dropped and excluded from the evaluation. The ICP algorithm is also equipped with a Cauchy filter (Cauchy parameter set to 1 m) and a maximum match distance filter ($d_{max} = 5$ m). These parameters are chosen according to common practices.

2) *Quantitative Comparison with Baselines:* We test our attack and the baselines on four Boreas repeat sequences. We repeat this across five perturbation bounds and document the results in Table I. Pose errors from ICP localizing original scans (i.e., scans without adversarial perturbations applied) are also included for reference.

It is evident that our model induces significant pose errors in ICP through adversarial perturbations. The original scans in the Boreas dataset contain numerous instances of occlusions and adverse weather, which are challenging environments for ICP. Nonetheless, perturbing each point by merely around 1 meter, our method induces pose errors that surpass those caused by the original scans in 99.7% of cases. Our approach surpasses the original even more frequently when bigger perturbations are allowed.

As the perturbation bound λ is not a hard constraint for our model, some perturbed points can overshoot this bound. To ensure a fair comparison with the baselines for which λ is a hard constraint, we give the baselines additional perturbation allowances. These allowances, ranging from 0.16 to 0.18 meters (i.e., 3.2% to 16% of λ), are empirically chosen for each sequence and perturbation bound pair. We verify that the additional allowances are larger or equal to our model’s overshoots 99.7% of the time. It is not 100% of the time due to the rare instances when our model’s perturbations significantly

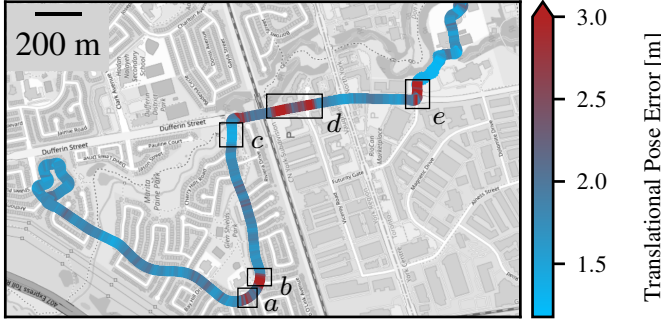


Fig. 4: Worst-case translation pose errors over a route estimated by our model when allowed up to 1 m of perturbation. Locations are coloured based on the magnitude of their worst-case translation pose error. Errors are capped at 3 m for better visualization. Some locations, such as *a*, *b*, *d*, and *e*, are much more prone to attacks than others such as *c*.

overshoot λ . The same thing is done for the experiments in Section IV-C.3. Often, the additional allowances we give to the baselines are much larger than our model’s overshoots. Therefore, the results in Table I are overcompensating for the baselines. Despite this, we can see that our method consistently outperforms the baselines by a big margin across different perturbation bounds. Allowed the same amount of perturbation as the baselines, our method learns non-trivial perturbations that lead to higher pose errors at least 88% of the time. This demonstrates the efficacy of our method as an attack and a tool for worst-case analysis.

3) *Pinpoint Dangerous Locations*: This section demonstrates how our approach can use autonomous driving datasets to identify dangerous locations that autonomous robots should avoid when deployed. Locations are dangerous if perturbations in the measurements can lead to large ICP errors. We apply our model to corrupt live scans collected over three Boreas repeat sequences that are over the same route but under different weather conditions. We set $\lambda = 1$ m as perturbations of 1 meter are realistic and can lead to severe pose errors. We plot the average translation pose errors induced at each location in Figure 4. Again, only longitudinal and lateral pose errors are considered. We notice that there are specific locations significantly more prone to attacks than others. At most locations, our model induces less than 2.2 meters of ICP errors. At locations coloured in red, our model can induce as much as 3 to 5 meters of ICP errors. We theorize that locations in red have very few landmarks upon which localization can rely. Prior work [9] pinpoints very similar dangerous spots in this trajectory and shows that these spots correspond to locations particularly vulnerable to corrupted measurements.

Locations *a*, *b*, *d*, and *e* in Figure 4 are examples of dangerous spots. All four locations are in the vicinity of parking lots, which provide very few landmarks for localization. Specifically, locations *a* and *b* are intersections in residential areas with small houses and a parking lot. Locations *d* and *e* have large parking lots on both sides of the road. In contrast, location *c*, which demonstrates high resilience to corruption in the measurements, has a number of trees on both sides.

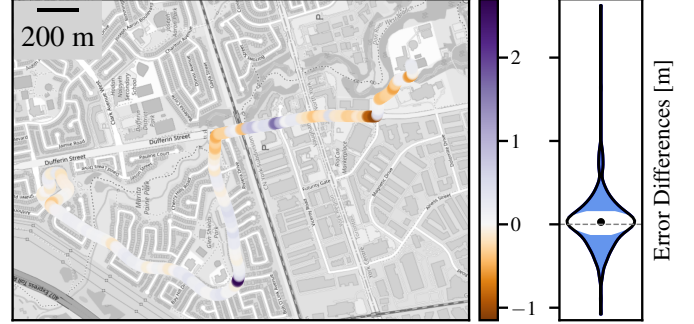


Fig. 5: ICP errors induced by our method minus those estimated by [9] on the same trajectory. A positive difference means ours finds a more detrimental perturbation pattern than [9]. $\lambda = 1$ m for both approaches. Left: the trajectory coloured by the error difference. Right: a violin plot of the distribution of differences, with the interquartile range denoted in white.

4) *Comparison with State-of-the-art*: This section compares our approach with [9] on a Boreas sequence. A closed-form solution for estimating the maximum ICP error that may result from a sector of measurement perturbations is presented in [9]. We propose an alternative solution that removes three assumptions made in [9]. First, while [9] only targets single-iteration ICP, this paper attacks the much more commonly used multi-iteration ICP. Second, our data association is recalculated at every ICP iteration, whereas [9] assumes a known data association. Third, while [9] does not consider robust filters, our approach can attack ICP with robust filters, making the attack more difficult. As our approach lacks the optimality guarantees [9] provides, we empirically demonstrate our approach’s effectiveness by comparing it to [9].

To enable comparison, [9] is extended to perturb the entire point cloud. At each location in the sequence, we compare ICP errors obtained from the two approaches, selecting the higher of the latitudinal and longitudinal errors, and visualize differences in the errors (ours minus [9]) in Figure 5. A positive difference means our approach finds a more detrimental perturbation pattern, leading to a higher ICP error.

The violin plot indicates that the two methods output similar errors in many places. At locations where they differ, [9] excels in more structured environments, such as highways with adjacent buildings, whereas ours performs better in unstructured environments. Additionally, we observe that our method outperforms [9] by a large margin at certain locations.

We theorize that, since [9] assumes single-iteration ICP with known data associations, it fails to capture the complexity of ICP in unstructured environments, as stated in their paper. Our method, which does not require these assumptions, can pinpoint dangerous unstructured environments prone to extreme, unusually high ICP errors. As such, our method provides a valuable complement by detecting the particularly hazardous locations the existing method [9] could overlook.

E. Generalization Capabilities

Our model showcases strong generalization capabilities to unseen data drawn from the same dataset. When trained on

only two Boreas sequences, our model generalizes well to other Boreas sequences with unseen weather conditions. Retraining is necessary when switching between datasets that are markedly different in point cloud pattern or density, such as from ShapeNet to Boreas. However, once retrained, our method demonstrates great attack performance across vastly different datasets, as shown previously.

V. CONCLUSION

In this paper, we propose the first learning-based attack against the widely used lidar-based ICP algorithm. Our attack learns how to perturb a point cloud to maximize the pose error when using ICP to localize it against a map. Our attack successfully induces significant pose errors in ICP and consistently outperforms baselines across different perturbation bounds in more than 88% of cases. We also demonstrate the feasibility of using our attack to analyze the resilience of ICP and estimate the worst-case pose errors ICP may encounter during deployment, where challenging situations such as occlusions and adverse weather can cause unusually high pose errors. As an example application of our framework, we can identify certain locations along a route that have significantly higher worst-case pose errors than others, highlighting vulnerabilities of ICP.

For future work, we would like to explore other types of corruption such as point addition and removal to cover more scenarios a robot can encounter during deployment. Furthermore, there is currently no enforcement that our model must generate perturbations that resemble real-world events. We will thus investigate using a discriminator to better simulate the effects of perturbations caused by common real events.

REFERENCES

- [1] P. Besl and N. D. McKay, "A method for registration of 3-D shapes," *IEEE Transactions on Pattern Analysis and Machine Intelligence*, vol. 14, no. 2, pp. 239–256, 1992.
- [2] F. Pomerleau, F. Colas, and R. Siegwart, *A Review of Point Cloud Registration Algorithms for Mobile Robotics*. 2015.
- [3] H. Yin, X. Xu, S. Lu, *et al.*, "A Survey on Global LiDAR Localization: Challenges, Advances and Open Problems," *arXiv preprint arXiv:2302.07433*, 2023.
- [4] K. Burnett, D. J. Yoon, Y. Wu, *et al.*, "Boreas: A multi-season autonomous driving dataset," *The International Journal of Robotics Research*, vol. 42, no. 1-2, pp. 33–42, 2023.
- [5] M. Pitropov, D. E. Garcia, J. Rebello, *et al.*, "Canadian Adverse Driving Conditions dataset," *The International Journal of Robotics Research*, vol. 40, no. 4-5, pp. 681–690, 2020.
- [6] C. Courcelle, D. Baril, F. Pomerleau, and J. Laconte, "On the Importance of Quantifying Visibility for Autonomous Vehicles under Extreme Precipitation," in *Towards Human-Vehicle Harmonization (Intelligent Vehicles and Transportation)*, Intelligent Vehicles and Transportation. 2023, vol. 3, pp. 239–250.
- [7] K. Burnett, Y. Wu, D. J. Yoon, A. P. Schoellig, and T. D. Barfoot, "Are We Ready for Radar to Replace Lidar in All-Weather Mapping and Localization?" *IEEE Robotics and Automation Letters*, vol. 7, no. 4, pp. 10 328–10 335, 2022.
- [8] Y. Endo, E. Javanmardi, and S. Kamijo, "Analysis of Occlusion Effects for Map-Based Self-Localization in Urban Areas," *Sensors*, vol. 21, no. 15, 2021.
- [9] J. Laconte, D. Lisus, and T. D. Barfoot, "Toward Certifying Maps for Safe Registration-Based Localization Under Adverse Conditions," *IEEE Robotics and Automation Letters*, vol. 9, no. 2, pp. 1572–1579, 2024.
- [10] A. X. Chang, T. Funkhouser, L. Guibas, *et al.*, "ShapeNet: An Information-Rich 3D Model Repository," *arXiv preprint arXiv:1512.03012*, 2015.
- [11] A. Censi, "An accurate closed-form estimate of ICP's covariance," in *Proceedings 2007 IEEE International Conference on Robotics and Automation*, 2007, pp. 3167–3172.
- [12] T. Tuna, J. Nubert, Y. Nava, S. Khattak, and M. Hutter, "X-ICP: Localizability-Aware LiDAR Registration for Robust Localization in Extreme Environments," *IEEE Transactions on Robotics*, vol. 40, pp. 452–471, 2024.
- [13] P. Babin, P. Giguère, and F. Pomerleau, "Analysis of robust functions for registration algorithms," in *2019 International Conference on Robotics and Automation (ICRA)*, 2019, pp. 1451–1457.
- [14] N. Charron, S. Phillips, and S. L. Waslander, "De-noising of lidar point clouds corrupted by snowfall," in *2018 15th Conference on Computer and Robot Vision (CRV)*, 2018, pp. 254–261.
- [15] J. Nubert, E. Walther, S. Khattak, and M. Hutter, "Learning-based localizability estimation for robust lidar localization," in *2022 IEEE/RSJ International Conference on Intelligent Robots and Systems (IROS)*, 2022, pp. 17–24.
- [16] J. Yang, Q. Zhang, R. Fang, B. Ni, J. Liu, and Q. Tian, "Adversarial Attack and Defense on Point Sets," *arXiv preprint arXiv:1902.10899*, 2019.
- [17] H. Zhou, D. Chen, J. Liao, *et al.*, "LG-GAN: Label Guided Adversarial Network for Flexible Targeted Attack of Point Cloud-based Deep Networks," in *Proceedings of the IEEE/CVF Conference on Computer Vision and Pattern Recognition*, 2020, pp. 10 356–10 365.
- [18] J. Sun, Y. Cao, Q. A. Chen, and Z. M. Mao, "Towards Robust LiDAR-based Perception in Autonomous Driving: General Black-box Adversarial Sensor Attack and Countermeasures," in *Proceedings of the 29th USENIX Conference on Security Symposium*, ser. SEC'20, USA: USENIX Association, 2020.
- [19] Q. Zhang, S. Hu, J. Sun, Q. Chen, and Z. Mao, "On Adversarial Robustness of Trajectory Prediction for Autonomous Vehicles," in *2022 IEEE/CVF Conference on Computer Vision and Pattern Recognition (CVPR)*, Los Alamitos, CA, USA: IEEE Computer Society, 2022, pp. 15 138–15 147.
- [20] W. Wang, Y. Yao, X. Liu, X. Li, P. Hao, and T. Zhu, "I Can See the Light: Attacks on Autonomous Vehicles Using Invisible Lights," in *Proceedings of the 2021 ACM SIGSAC Conference on Computer and Communications Security*, ser. CCS '21, New York, NY, USA: Association for Computing Machinery, 2021, pp. 1930–1944.
- [21] Y. Xu, X. Han, G. Deng, J. Li, Y. Liu, and T. Zhang, "SoK: Rethinking Sensor Spoofing Attacks against Robotic Vehicles from a Systematic View," in *2023 IEEE 8th European Symposium on Security and Privacy (EuroS&P)*, 2023, pp. 1082–1100.
- [22] K. Yoshida, M. Hojo, and T. Fujino, "Adversarial Scan Attack against Scan Matching Algorithm for Pose Estimation in LiDAR-Based SLAM," *IEICE Transactions on Fundamentals of Electronics, Communications and Computer Sciences*, vol. E105.A, no. 3, pp. 326–335, 2022.
- [23] D. Lisus, J. Laconte, K. Burnett, and T. D. Barfoot, "Pointing the Way: Refining Radar-Lidar Localization Using Learned ICP Weights," *arXiv preprint arXiv:2309.08731*, 2023.
- [24] T. D. Barfoot, *State Estimation for Robotics*. 2023.
- [25] C. R. Qi, L. Yi, H. Su, and L. J. Guibas, "PointNet++: Deep Hierarchical Feature Learning on Point Sets in a Metric Space," in *Proceedings of the 31st International Conference on Neural Information Processing Systems*, ser. NIPS'17, Long Beach, California, USA: Curran Associates Inc., 2017, 5105–5114.
- [26] X. Yan, "Pointnet/Pointnet++ Pytorch," https://github.com/yanx27/Pointnet_Pointnet2_pytorch, 2019.
- [27] N. Wang, Y. Zhang, Z. Li, Y. Fu, W. Liu, and Y.-G. Jiang, "Pixel2Mesh: Generating 3D Mesh Models from Single RGB Images," in *ECCV*, 2018.
- [28] P. T. Furgale and T. D. Barfoot, "Visual Teach and Repeat for Long-Range Rover Autonomy," *Journal of Field Robotics, special issue on "Visual mapping and navigation outdoors"*, 2010.
- [29] I. Loshchilov and F. Hutter, "Decoupled Weight Decay Regularization," in *7th International Conference on Learning Representations, ICLR 2019, New Orleans, LA, USA*, 2019.
- [30] A. V. Segal, D. Hähnle, and S. Thrun, "Generalized-ICP," in *Robotics: Science and Systems*, 2009, pp. 168–176.

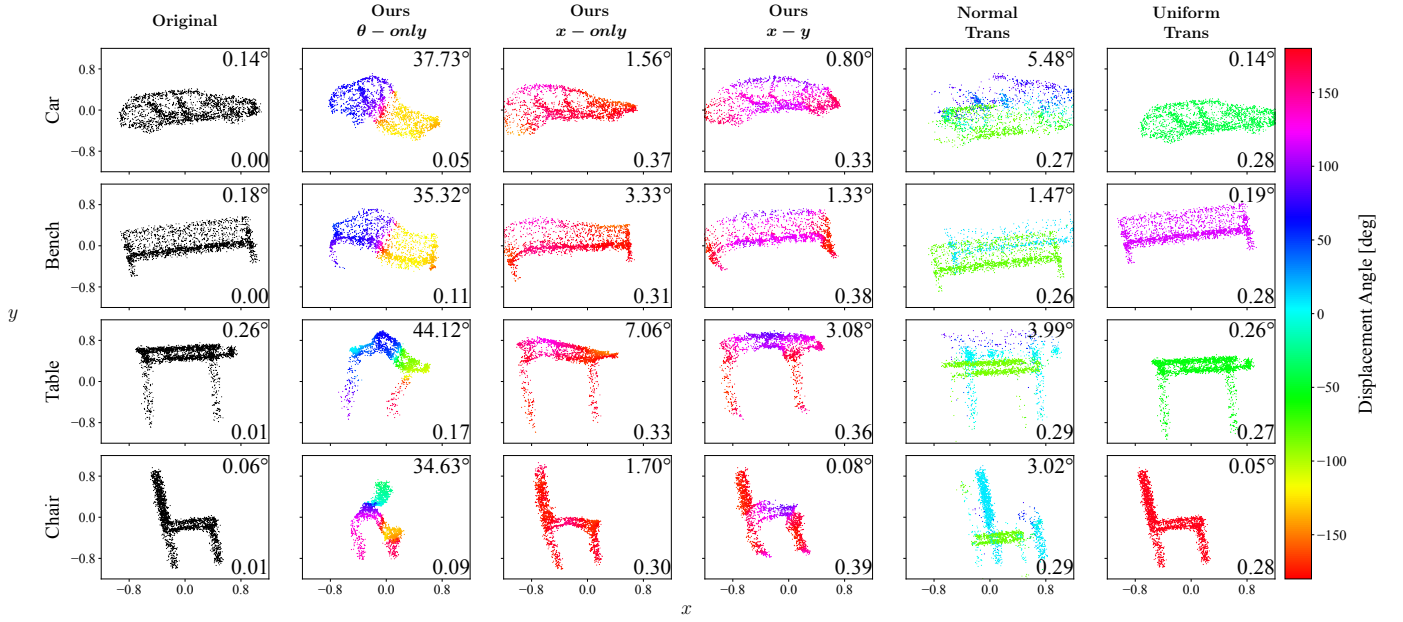


Fig. 6: An extended comparison between the original point clouds and the adversarial point clouds produced by our model and the baselines. Columns 2 through 6 showcase the adversarial point clouds resulting from applying our models and the baselines to the original point clouds in column 1. The adversarial point clouds are coloured according to the angle of the displacement vectors, $\mathbf{X}_{\text{adv}} - \mathbf{X}$. The heading pose error and the norm of the lateral and longitudinal pose errors of ICP induced by each point cloud are indicated at the upper and lower right corners, respectively. The lateral and longitudinal pose errors are unitless as the point clouds are normalized. Minor ICP pose errors are observed even when localizing the uncorrupted point clouds in column 1. This occurs because noise is added to the scans to prevent perfect alignment between the scans and the maps.

APPENDIX

A. Extended ShapeNetCore Results

Extended ShapeNetCore [10] results are shown in Figure 6.